RESEARCH ARTICLE

Fabrication of Microstructured Calcium Phosphate Ceramics Scaffolds by Material Extrusion-Based 3D Printing Approach

Peifang Dee[1,2], Sharlene Tan[1], Hortense Le Ferrand[1,2,3]*

[1]School of Mechanical and Aerospace Engineering, Nanyang Technological University, Singapore 639798, Singapore
[2]Singapore Centre for 3D Printing, Nanyang Technological University, Singapore 639798, Singapore
[3]School of Materials Science and Engineering, Nanyang Technological University of Singapore, 50 Nanyang Avenue, Singapore 639798, Singapore

Abstract: Natural materials such as bone and enamel have intricate microstructures with inorganic minerals oriented to perform multiple mechanical and biological functions. Current additive manufacturing methods for biominerals from the calcium phosphate (CaP) family enable fabrication of custom-shaped bioactive scaffolds with controlled pore structures for patient-specific bone repair. Yet, these scaffolds do not feature intricate microstructures similar to those found in natural materials. In this work, we used direct material extrusion to 3D print water-based inks containing CaP microplatelets, and obtained microstructured scaffolds with various designs. To be shear-thinning and printable, the ink incorporated a concentration of 21 – 24 vol% CaP microplatelets of high aspect ratio. Good shape retention, print fidelity and overhanging layers were achieved by simultaneous printing and drying. Combined with the 3D design, versatile CaP microstructured objects can be built, from porous scaffolds to bulk parts. Extruded filaments featured a core-shell microstructure with graded microplatelet orientations, which was not affected by the printing parameters and the print design. A simple model is proposed to predict the core-shell microstructure according to the ink rheology. Given the remaining open porosity after calcination, microstructured scaffolds could be infiltrated with an organic phase in future to yield CaP biocomposites for hard tissue engineering.

Keywords: Robocasting; Calcium phosphate; Microstructure

*Correspondence to: Le Ferrand Hortense, School of Mechanical and Aerospace Engineering, Nanyang Technological University, Singapore 639798, Singapore; hortense@ntu.edu.sg

Received: December 23, 2021; **Accepted:** February 26, 2022; **Published Online:** February 26, 2022

Citation: Dee P, Tan S, Le Ferrand H., 2022, Fabrication of Microstructured Calcium Phosphate Ceramics Scaffolds by Material Extrusion-Based 3D Printing Approach. *Int J Bioprint,* 8(2):551. http://doi.org/10.18063/ijb.v8i2.551

1. Introduction

Natural materials such as bone and enamel possess highly complex microstructures featuring calcium phosphate (CaP) rods or platelets oriented in multiple directions[1,2]. These complex microstructural patterns are thought to contribute to the outstanding mechanical and functional properties of these natural materials[3,4]. In bone, for example, the local alignment of CaP anisometric nanoplatelets in an organic phase results in a combination of toughening mechanisms that increase crack resistance and prevent brittle fracture[4]. Indeed, using the tension-shear chain model, fracture mechanics theoretically predicts that high aspect ratio CaP platelets with nanoscale thickness do not break, but experience pull-out from the protein-matrix[3]. At present, numerous bone repair materials have been developed, including bioactive glasses, hydroxyapatite composites, bone cements, and polymers[5-7]. Among these, CaP-based scaffolds are promising due to similar chemical composition with natural bone. Furthermore, additive manufacturing, also called three-dimensional (3D) printing, is now extensively used to fabricate 3D scaffolds enabling vascularization, cell invasion, and bone growth[8,9]. However, these synthetic bone implant materials lack the complex microstructures

found on their natural counterparts[10,11]. Developing 3D printed CaP scaffolds with a complex microstructure could induce more biomimetic properties. For example, the microstructure could be designed to increase crack resistance and impart anisotropic mechanical properties to CaP scaffolds. Therefore, new 3D printing strategies are needed to allow the fabrication of CaP materials with controlled shape and design as well as an internal microstructure.

Conventional fabrication methods to synthesize microstructured CaP include biotemplating, freeze-casting, and lamination. In biotemplating, natural porous microstructured materials such as cuttlefish bone[12] or rattan wood[13-16] are decellularized then remineralized with CaP by a hydrothermal treatment. Through this way, the original porous hierarchical microstructure of the natural material is preserved in the synthetic material. In freeze-casting, also called ice-templating, the microstructure is induced by the directional growth of ice dendrites during freezing[17-19]. When subjecting slurries containing ceramic particles to freeze-casting, the growing ice dendrites push and shear the particles, leading to the increase in local packing of particles. When the particles are anisometric, self-assembly and particle alignment are also reported[20]. After removing the ice dendrites by sublimation, a lamellar ceramic scaffold with elongated pores oriented in desired directions is obtained. This method can be combined with external fields or temperature gradients to control the microstructure and shape. For example, bidirectional freezing of a hydroxyapatite suspension produced a biomimetic, nacre-like microstructure with enhanced mechanical properties[21]. Besides, microstructured CaP materials can be built using lamination from sheets of CaP platelets or whiskers. For example, a nacre-like composite was made by laminating alginate films containing CaP microplatelets[22]. A twisted plywood or Bouligand microstructure could also be made using CaP microfibers, leading to significant enhancement in the toughness of the composite[23]. Unfortunately, these methods are not yet easily compatible with 3D printing, which is required to provide patient-adapted shapes and tunable designs of internal pore structures[10,24].

3D printed CaP scaffolds have demonstrated promising osteogenic ability for bone tissue engineering and research has been growing[10,24]. In particular, direct material extrusion (or robocasting) and indirect vat photopolymerization-based techniques have been the most extensively used for CaPs. In an interesting example which applied photopolymerization after material extrusion with cell seeding, an ultraviolet (UV)-curable hydrogel scaffold was bioprinted with only up to 30 wt% nanocrystalline CaPs formed by *in situ* precipitation, which contributed to the scaffold's compressive strength through electrostatic interaction with the polymers and were not cytotoxic to fibroblasts[25]. Although there has been no 3D printed microstructured CaP scaffolds, 3D printing of other microstructured ceramics have been reported, often using alumina microplatelets of high aspect ratio. Digital light processing (DLP) was used to create various architectures from alumina microplatelets suspended in a UV-curable resin using magnetic alignment[26]. The alumina microplatelets were pre-coated with iron oxide nanoparticles so that the microplatelet orientation could be controlled by magnetic fields applied during DLP. While the local control over the alumina microstructure was precise, the composite had a low mineral content of only 15 vol%)[26]. Alternatively, direct extrusion of alumina microplatelets was used to induce alignment by shear[27,28]. Alumina filaments with a core-shell microstructure were robocast to form a twisted plywood structure[27]. The pluronic-based gel containing 31 vol% alumina microplatelets and microparticles produced green bodies with 36 vol% residual porosity after drying and isostatic pressing[27]. Higher sintering temperatures could further reduce the final porosity through templated grain growth, whereby the surrounding alumina nanoparticles enhanced grain growth and densification of the aligned alumina platelets without affecting the microstructure[28,29]. While vat photopolymerization-based approaches such as DLP achieve higher resolution and better surface finish than direct extrusion[10,30], the volume fraction of particles which can be suspended in the photocurable resin is limited by the increase in viscosity. In vat photopolymerization, the low ceramic content makes printed parts prone to cracking and shrinkage during debinding and sintering[10,30]. Direct material extrusion, on the other hand, can yield higher concentrations of solid particles in the green body. Continuous filament extrusion could therefore be applied to an ink composition containing anisometric CaP minerals with the microstructure controlled using shear stresses. Along with the microstructure, controllable macroscopic porosity as found in conventional bone scaffolds would also be required in 3D printed structures to allow vascularization and cell invasion. Such porous structures have not been reported with the microstructured alumina printing.

In this work, we 3D print microstructured CaP parts by direct ink writing (DIW), based on line-by-line material extrusion. The microstructure is created by orienting synthesized brushite ($CaHPO_4 \cdot 2H_2O$) microplatelets suspended in a water-based ink using shear stresses that develop in the printing nozzle. The ink is designed to allow simultaneously efficient particle alignment and high solid loading after printing, of about 23 vol%. The strategy to create complex shapes is to simultaneously dry while depositing the ink onto a porous gypsum substrate that sucks out water from the deposited ink through capillary

forces. The CaP parts could later be consolidated with the microstructure retained by calcination at a temperature lower than the sintering temperature. First, we study the rheological properties of aqueous inks at various solid loadings of brushite and assess the printability to obtain a good print resolution. Then, we analyze the microstructure of extruded filaments and use a simple model to relate the microstructure to the rheology of the ink. Finally, we demonstrate that complex, porous or bulk 3D shapes can be obtained with our approach, such as scaffolds or bone plates. This work is anticipated to be of interest for fabricating patient-adapted implants with more biomimetic microstructure to enable enhanced properties. Future work could tackle infiltration of the 3D printed CaP scaffolds with a biomimetic polymeric matrix to study the mechanical properties and the cellular response.

2. Materials and methods

2.1. Synthesis and characterization of brushite microplatelets

Brushite microplatelets were prepared using a method described by Gao *et al*.[22] and Mandel and Tas[31]. Briefly, 6.062 g of calcium chloride ($CaCl_2$) (anhydrous, ≥97%, Sigma) dissolved in 0.4 L of deionized water was rapidly added to a beaker with 1.650 g of potassium dihydrogen phosphate (KH_2PO_4) (anhydrous, ≥99% ACS, VWR Chemicals, Singapore) and 6.026 g of disodium hydrogen phosphate (Na_2HPO_4) (anhydrous, ≥99% ACS, VWR Chemicals, Singapore) dissolved in 1.4 L of deionized water. After stirring at room temperature for 1 h, the white precipitate was collected by vacuum filtration and dried in a 45°C oven for 2 days. 6.062 g $CaCl_2$ in 1.8 L reaction mixture produced a yield of ~7.0 g brushite. The synthesis is easily scalable, with a yield of ~10.6 g brushite collected from 2.7 L reaction mixture using 9.093 g $CaCl_2$. The powder was stored in a dry box until use.

The synthesized powder was sputtered with gold and examined under a field emission scanning electron microscope (SEM) (JEOL 6340F) to determine its dimensions. The powder was grinded using mortar and pestle and characterized using powder X-ray diffraction (XRD) with Bragg-Brentano geometry (Panalytical X'Pert Pro, Cu K_α 0.1541874 nm, scanning range 2θ from 10° to 60°, step size 0.017°). The scanned material was checked against the PDF-4+ database (2021) using Match! (version 3.6, Crystal Impact). Reference CIF files obtained from the Inorganic Crystal Structure Database (ICSD, FIZ Karlsruhe) was used for analysis in TOPAS (version 6, Bruker AXS). Energy dispersive spectroscopy (EDS) was performed on coated powder in a thermionic SEM (JEOL 5500LV) with Oxford Inca 200 detector, 20 kV accelerating voltage) to measure the calcium/phosphorus atomic ratio.

2.2. Preparation and characterization of the brushite ink

The aqueous brushite ink consisted of various volume fraction Φ of brushite microplatelets, an anionic surfactant Dolapix CE 64 (Zschimmer & Schwarz, Germany) as the dispersant, and polyvinylpyrrolidone (PVP) of average molecular weight ~360,000 (Sigma-Aldrich) as the binder. Synthesized brushite powder was slowly added to deionized water containing 0.1 wt% Dolapix CE 64 with respect to brushite, frequently mixing with vortex and probe sonicator (Bandelin), resting 2 s between every 1 s of low amplitude ultrasonic pulse to prevent overheating. 20 w/v% PVP stock solution was added to the suspension to give a final concentration of 7 w/v% PVP with respect to water. The brushite ink was homogenized by mixing with vortex and probe sonicator before use.

The rheological properties of the inks were measured using a rheometer (Bohlin, Malvern Instruments) and 15 mm serrated plates. All measurements were performed at room temperature with a gap of 1000 μm. An amplitude sweep from 0.1 Pa to 1000 Pa was carried out in oscillatory mode at 1 s^{-1}. Rotational measurements were carried out from 0.01 s^{-1} to 100 s^{-1}. All measurements were repeated at least three times.

2.3. Drying of brushite ink

The possibility of drying extruded brushite inks by solvent removal through a water-absorbent print substrate was studied using gypsum, also known as plaster of Paris. Gypsum is an abundant, safe, and easily moldable material. Gypsum was prepared by mixing 6 parts water to every 10 parts gypsum casting powder (Cera-Mix Standard Plaster Casting Compound) by weight. To obtain a flat gypsum substrate, the gypsum slurry was cast onto a non-stick surface and mechanically smoothed at the top by pressing with a flat surface while wet, then left overnight to set.

A 5 μL droplet of 21 vol% brushite ink was deposited on the gypsum slab with a micropipette. A digital microscope (Dino-Lite Edge AM7915MZTL) was used to record videos of the droplet drying on the gypsum substrate. The droplet size and contact angle were measured from the video snapshots using ImageJ. The experiment took place at an ambient temperature of ~22°C and relative humidity ~74%.

2.4. Direct material extrusion of brushite

For 3D printing, the brushite ink was filled into a 10 mL Luer-lock syringe (Terumo) of inner diameter 14.3 mm. Cone-shaped polyethylene nozzles (Nordson EFD Optimum SmoothFlow) were used. The syringe was fitted to a clay printer (3D Potterbot Micro 8, USA) using a custom adapter to enable mechanical extrusion of

filaments by pushing the plunger down, and the plunger speed was measured. The printer stage moved in the $-x$ direction at the printing speed v. To print the first layer, the nozzle tip was set at 0.6 mm (z_1) above the print substrate. The nozzle tip moved up by 0.5 mm (z_2) every subsequent layer. A spirit level was used to ensure the print substrate was level. The setup is shown in **Figure 1** and the printing parameters are described in **Table 1**.

When building structures taller than 3 mm, a hot plate may be secured on the printer stage directly under the print substrate to enable quick drying of the water-based ink during printing. The print substrate surface was heated to 85 – 95°C.

2.5. Post-processing of 3D printed parts and chemical characterization

The printed parts were left to dry in ambient conditions overnight before detaching them from the gypsum substrate from one edge by sliding in a sharp blade.

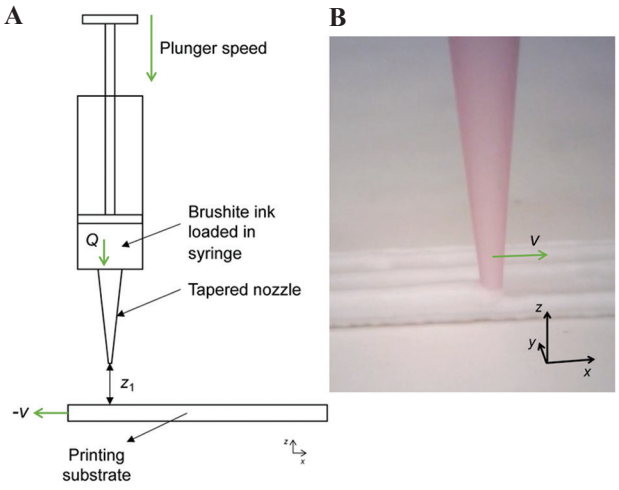

Figure 1. (A) 3D printing setup and parameters, as described in **Table 1.** (B) Close-up photograph near the nozzle tip (d = 0.58 mm).

Alternatively, elective pre-treatment in a 200°C oven for 4 h may be performed before detaching the print from the substrate. The green parts underwent debinding at 500°C for 2 h and calcination at 900°C for 6 h in a box furnace (Nabertherm, Germany) using a heating ramp of 5°C/min. The samples were left to cool in the furnace to prevent cracking during shrinkage. To determine the crystallographic phase transformation of the CaP after calcination, the material was crushed into powder and analyzed by XRD using the same procedure as previously described in section **2.1**.

2.6. Characterization of the prints

Cross-section surfaces of calcined parts exposed by brittle fracture were observed under thermionic SEM (JEOL 5500LV) after coating with gold. Alternatively, calcined parts were embedded in resin and polished to examine the microstructure under the SEM. The microplatelet orientations in the prints were determined by image analysis using ImageJ v1.53g.

3. Results and discussion

3.1. 3D printing approach

Our 3D printing approach (**Figure 2**) utilizes CaP microplatelets of high aspect ratio suspended in an aqueous slurry, which is extruded onto a porous water-absorbent substrate for drying and consolidation. The bioceramic chosen in the water-based ink is brushite ($CaHPO_4 \cdot 2H_2O$), a type of CaP also known as dicalcium phosphate dihydrate (DCPD). Brushite microplatelets can be synthesized in scalable quantities and yield a bioresorbable material, calcium pyrophosphate, after calcination[32] (**Supplementary file: Section 1.1** for details about the crystallographic phase). Here, the aspect ratio of the synthesized brushite was large, with microplatelets of ~10 μm length and ~13.8 nm

Table 1. Printing parameters descriptions and settings used

Printing parameter	Description	Settings used
Q	Volumetric flow rate of ink extrusion	Plunger speed multiplied by the cross-sectional area of the syringe
d	Inner diameter of nozzle tip	0.41, 0.58, 0.84, 1.19, and 1.60 mm
f	Multiplier for ink flow rate Q	500 and 800%
v	Speed of nozzle relative to the printing substrate in the x-direction	1, 5, and 10 mm/s
I_f	Infill density controlling how densely the part volume is filled with ink	30%, 50%, 70%, and 90%
Extrusion width	Multiplier for extruded filament width	Fixed at 100%
z_1	Initial stand-off distance of nozzle tip above printing substrate	0.6 mm (first layer)
z_2	Height increment of nozzle tip	Fixed at 0.5 mm (subsequent layers)

thickness (see **Supplementary file: Section 1.2**). These dimensions were chosen because microplatelets with nanoscopic thickness are thought to be optimal to achieve platelet pull-out instead of brittle fracture in bioinspired microstructured composites[3]. The ink solvent was water to allow good dispersion and high concentration of brushite microplatelets. An anionic surfactant was used as dispersant and PVP was used as the binder to strengthen the green part after drying. The printed parts were dried overnight before calcination at 900°C for a dwell time of 6 h to yield a stiff, consolidated part. The arrangement of microplatelets within the printed filaments remained intact as the low calcination temperature of 900°C prevented necking and shrinkage, while ensuring complete phase transformation into β-calcium pyrophosphate (β-CPP, $Ca_2P_2O_7$)[32] (**Supplementary file: Section 1.1**). After printing, drying, and calcinating, the CaP material has a relative density of about 23 vol%.

The key to enabling extrusion at the nozzle, microstructuring and high relative density in the final material resides in the optimization of the brushite solid content in the ink, whereas the realization of complex, 3D shapes is governed by the fast drying of the ink on the porous substrate. How to determine the ink composition and its printability are detailed in the following section.

3.2. Rheology and printability of brushite inks

The rheological properties of inks were tested to determine the required brushite solid loading Φ (**Figure 3**). The primary property that had to be achieved is flowability to enable extrusion through a nozzle. To this aim, brushite inks with solid loadings from 16 to 27 vol% were tested in viscometry (**Figure 3A**). As expected, the apparent viscosity of the inks increased with the concentration of brushite. In particular, the ink with 27 vol% brushite was paste-like, with an increased viscosity at rest of 600 Pa·s (see **Supplementary file: Section 2**). Furthermore, the ink gradually shifted from a zero-shear viscosity profile at lower solid loadings to a yield stress profile at the highest solid loading of Φ = 27 vol% (**Figure 3A**). The inks were modeled as Herschel-Bulkley fluids and their flow profiles from 10 s^{-1} to 100 s^{-1} were fitted with:

$$\tau = \tau_y + K\gamma^n \tag{3.1}$$

where τ is the shear stress (Pa), τ_y the yield stress (Pa), the shear rate (s^{-1}), K the consistency index and n the flow index[28,33]. All inks had a flow index $n < 1$, confirming their shear-thinning properties, which is necessary for the extrusion (**Figure 3B**). Also as expected, the consistency increased with solid loading, denoting less fluidity as more brushite particles are loaded in the ink. These data suggest that all inks can be extruded through a nozzle. However, a yield stress of 100 ~ 800 Pa is typically reported as one of the printability criteria for extruded filaments to support their own weight and avoid sagging[34]. From Equation 3.1, only the ink containing 27 vol% CaP microplatelets exhibits a yield stress. Another important rheological property is the stiffness of the ink at rest indicated by G'_{eq}, which is the plateau value of the storage modulus before the yield point[28,34]. Printable ceramic inks typically have G'_{eq} at rest ranging from 25 to 200 kPa and a damping factor at rest G''_{eq}/G'_{eq} ranging from 0.1 to 0.3[34]. These properties are key to realizing shape fidelity. The viscoelastic properties of brushite inks at various solid loadings were thus measured. In all of our brushite inks, liquid-like behavior generally dominated with damping factor $G''/G' > 1$, even for 27 vol% which

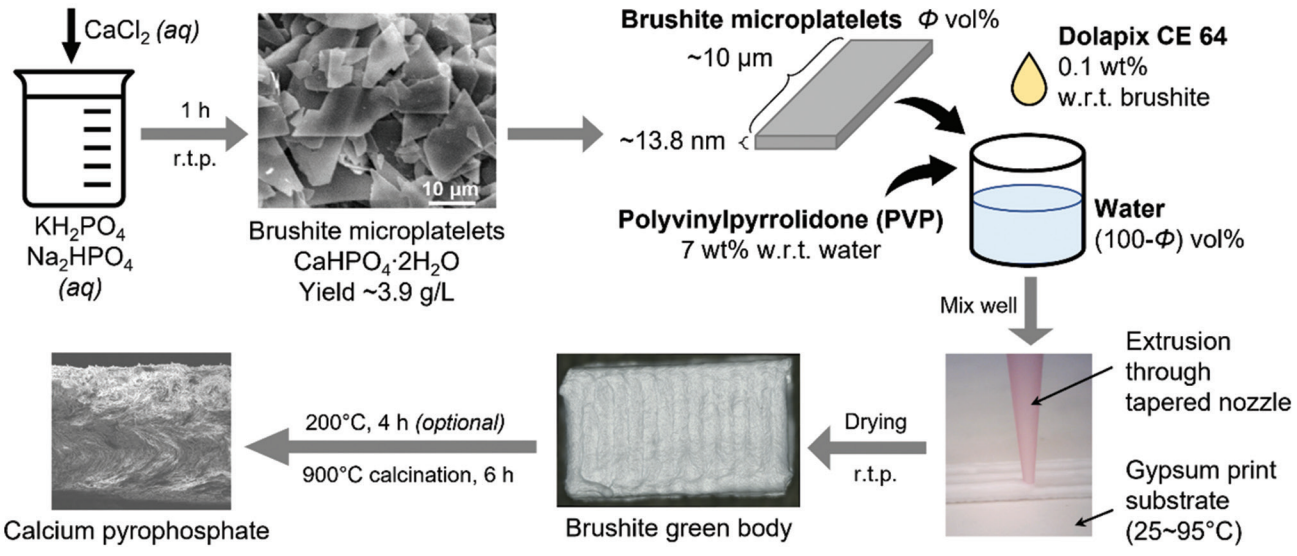

Figure 2. Schematic of the 3D printing strategy: scalable synthesis of brushite microplatelets of high aspect ratio loaded into an aqueous-based ink. The ink is 3D printed by direct extrusion onto porous substrate, before drying and calcination to yield a solid, microstructured part.

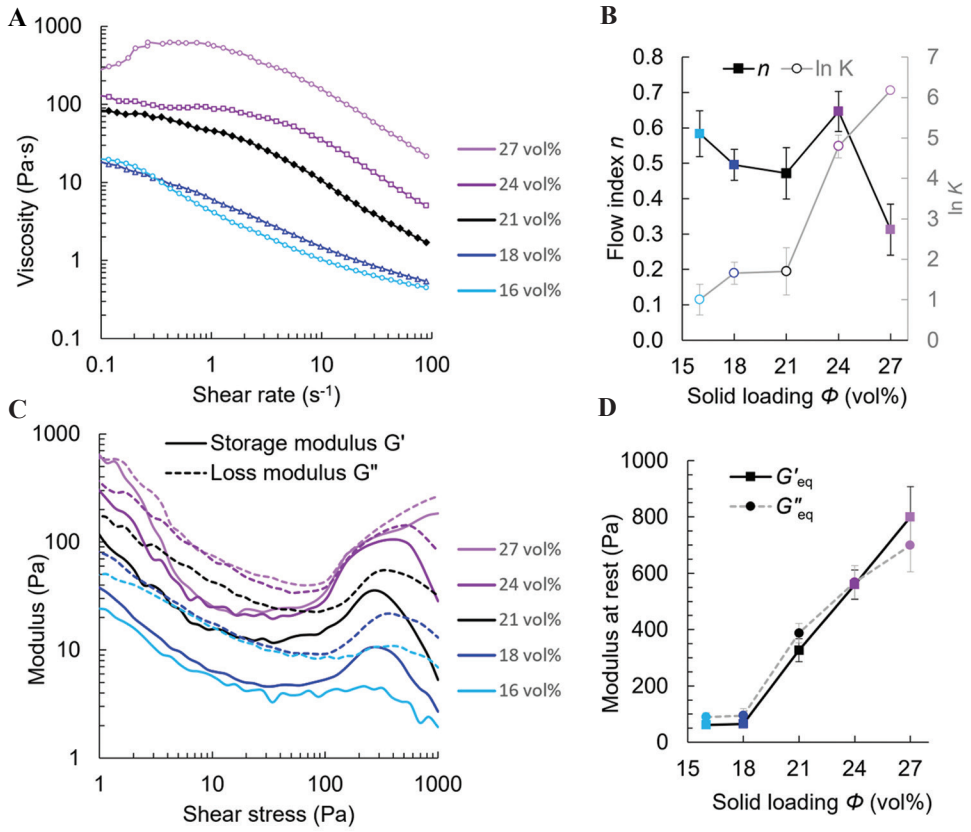

Figure 3. Rheological properties of brushite inks with solid loading Φ = 16 to 27 vol%. (A) Representative viscosity profile as a function of the shear rate. (B) Flow index n and ln K as a function of brushite solid loading. (C) Representative storage modulus G' and loss modulus G'' as a function of the shear stress. (D) G'_{eq} and G''_{eq} as a function of the brushite solid loading.

had a paste-like consistency (**Figure 3C**). The initial G'_{eq} at rest increased with Φ but remained below 1 kPa for all inks (**Figure 3D**). This suggests that none of the inks presents the rheological properties typically required for direct extrusion.

To overcome the absence of yield stress and the low stiffness of the inks, the printing strategy involves drying the ink as it is printed by using a porous print substrate. This approach is inspired from ceramic slip casting where a liquid slurry, generally water-based, is poured into a porous substrate that sucks out the water by capillary action[35]. Using the brushite ink with solid loading of 21 vol%, we demonstrated that drying is a good approach for shape retention and fidelity. The drying was carried out by placing a porous flat slab of gypsum, similar to those used in slip casting, as a water-absorbent print substrate. On extrusion onto the gypsum substrate, the water from the ink is rapidly absorbed by capillary action, increasing the solid loading of the printed filament and maintaining its shape, as illustrated with the droplet of 21 vol% brushite ink (**Figure 4A**). Furthermore, shape retention was achieved: on depositing the sessile droplet, the contact angle remained high at about 111 – 113°, while the droplet dries. The use of the gypsum substrate indeed restricts the spreading of liquid ink, thereby enabling shape fidelity. Besides, the drying of the ink droplets at ambient room temperature and >70% relative humidity typically leveled off after about half a minute, hence enabling sufficiently fast 3D printing of under one minute per layer.

Testing the inks of various solid loadings, we found that inks with $\Phi \leq 18$ vol% were not easily extrudable with uniform thickness and often produced discontinuous filaments (**Figure 4B**). We also found that the ink containing 27 vol% brushite tended to clog nozzles and exhibited more print defects compared to the other concentrations. 21 and 24 vol% brushite inks are therefore adequate. In the remainder of the paper, the brushite ink containing 21 vol% brushite will be used to study the microstructure development in the 3D printed scaffolds. The results can be extrapolated for the ink containing 24 vol% brushite, if needed.

3.3. Filament size and microstructure

(1) Filament shape fidelity and size

The microstructure in the 3D printed materials built from 21 vol% brushite ink was characterized after consolidating the print by calcination at 900°C. The effects of the print

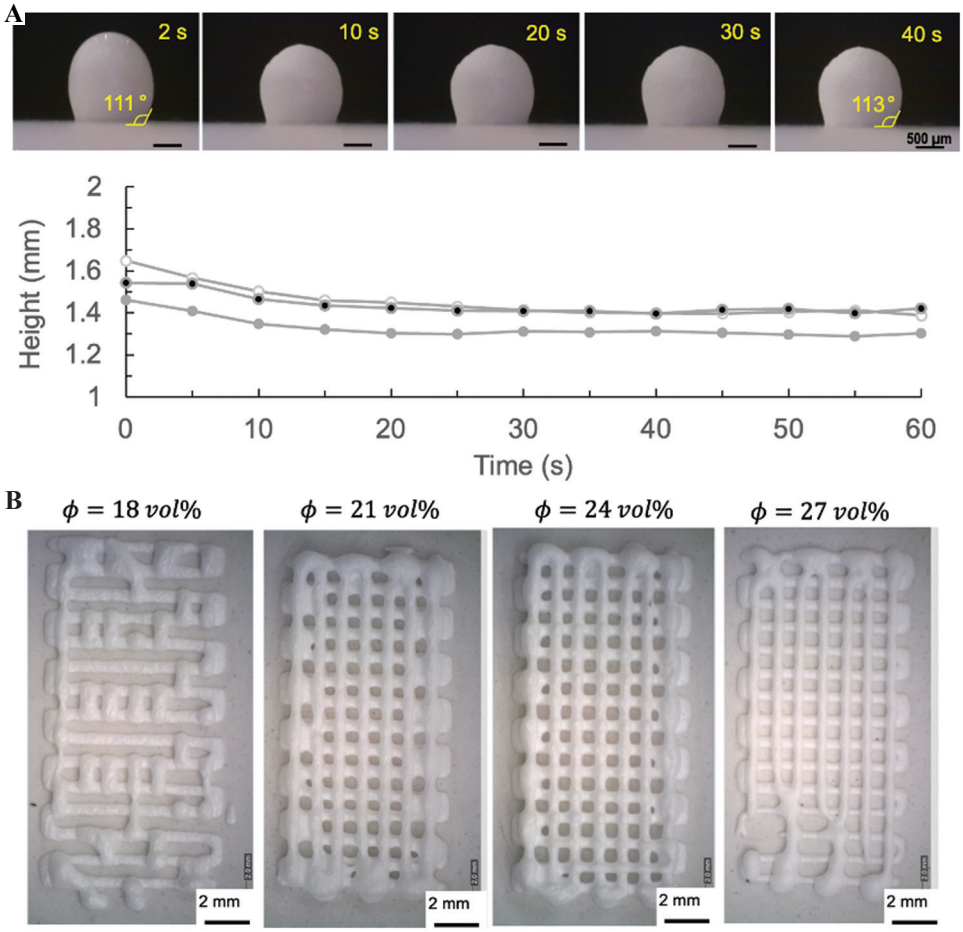

Figure 4. (A) Optical images showing the drying of a 5 µL droplet of 21 vol% brushite ink on gypsum substrate and measurement of the height of the droplets as a function of time. Contact angle remains almost unchanged during drying. Scale bar is the same on all images (0.5 mm). (B) Optical images of printed structures using the inks with various solid loadings at room temperature.

parameters on the shape fidelity and microstructure were first studied on single printed lines, which are also referred to as "filaments." Single filaments were extruded through nozzles of different sizes at a flow rate multiplier f = 500% or f = 800% and a printing speed v = 1 mm/s to 10 mm/s. The size of the nozzle was the primary parameter studied since it is known that the flow through a pipe is laminar and has a parabolic profile along the diameter of the pipe:

$$v(r) = v_c \cdot \left(1 - \left(\frac{r}{d}\right)^2\right) \quad (3.2)$$

where v is the flow in a pipe of diameter d, v_c is the flow at the center of the pipe and r is the position along the diameter. The flow rate multiplier was also tuned as it controlled the volume flow rate of the fluid through the nozzle, whereas the printing speed was maintained constant to allow for 3D printing of continuous lines. After calcination, filament cross-sections were examined under SEM to measure their dimensions and their microstructure (width, w, area of filament, A and area of filament core, C) (**Figure 5**). The shape of the cross-section of filaments extruded on gypsum typically resembled the outline of the ink droplet dried on gypsum shown in **Figure 4A**. A high contact angle and a round-like shape were obtained (**Figure 5A**). Looking at the cross-section, a core-shell microstructure appeared with a core region C showing disordered microplatelets, whereas the shell had microplatelets aligned along the border of the filament (**Figure 5A and B**).

The cross-section area of an extruded brushite filament is expected to exceed the area of the nozzle tip due to the pressure drop experienced by the ink on exiting the nozzle[36]. The cross-section area A of the calcined filament was observed to increase linearly with nozzle diameter d (**Figure 5C**). A also scales linearly with the flow rate f. In addition, the final filament width w was found to have a linear relationship with $\sqrt{d \times f}$ (**Figure 5D**). Although these relationships are empirical, they are convenient as they permit simple adjustment of the flow rate multiplier f according to the desired resolution, for a given nozzle size.

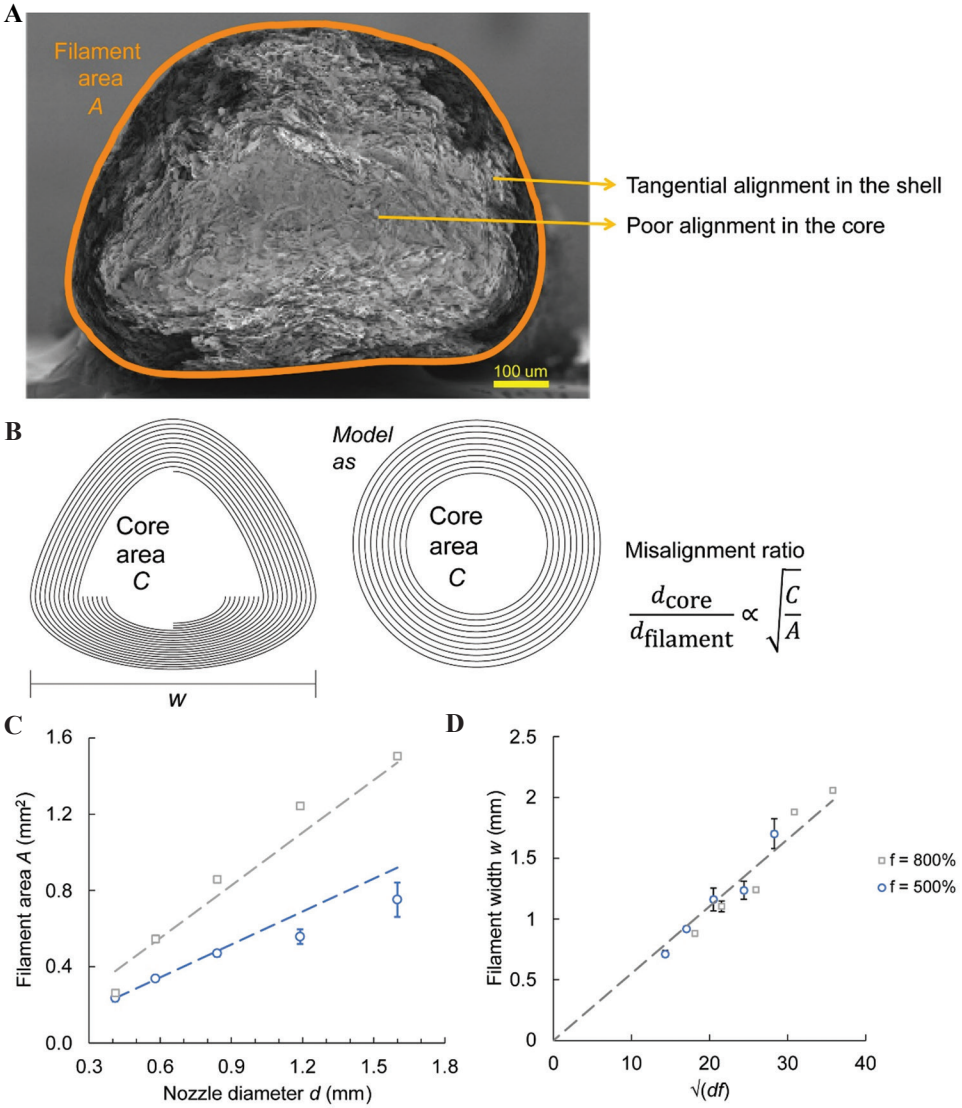

Figure 5. (A) Electron micrographs of the cross-section of a filament extruded though 0.58 mm nozzle at f = 500% after calcination, showing cross-section area A (orange) and the core-shell microstructure. Scale bar: 100 µm. (B) Schematic showing the idealized model of a typical filament cross-section. Post-calcination dimensions of filaments extruded through different nozzle diameters d at f = 500% and at f = 800%. (C) Cross-section area A of filaments extruded from different sized nozzles. (D) Width w of final filaments. Dashed line shows prediction that w is proportional to $\sqrt{(df)}$.

(2) Filament microstructure

After looking into the effect of the print parameters on the print resolution, the core-shell microstructure is analyzed (**Figure 6**). Near the filament edge, the microplatelets were aligned tangentially forming a distinctive "shell," whereas the microplatelets at the filament "core" exhibited poor alignment (**Figure 5A and B**). These observations share similarities with previous works on extrusion of alumina platelets through straight nozzles[24,25]. During extrusion, the shear stresses in the nozzle aligned the microplatelets tangentially, especially those close to the filament edge where the stresses are higher. In this way, the characteristic core-shell microstructure as observed from the y-z cross-section is produced. The area of the filament core region C was measured from electron micrographs (**Figure 5A and 5C**). The relative core radius to filament radius after calcination is approximated by $\sqrt{C/A}$, hereby called the misalignment ratio. We used the area instead of the height or width as the filament obtained did not have a perfectly round cross-section (**Figure 5B**). Despite variations in the filament diameter, the misalignment ratio of CaP filaments remained approximately constant at about 0.68 with the nozzle size d, flow rate multiplier f, and printing speed v (**Figures 6A and B**). Unchanged misalignment ratio at different nozzle diameter has also been reported in

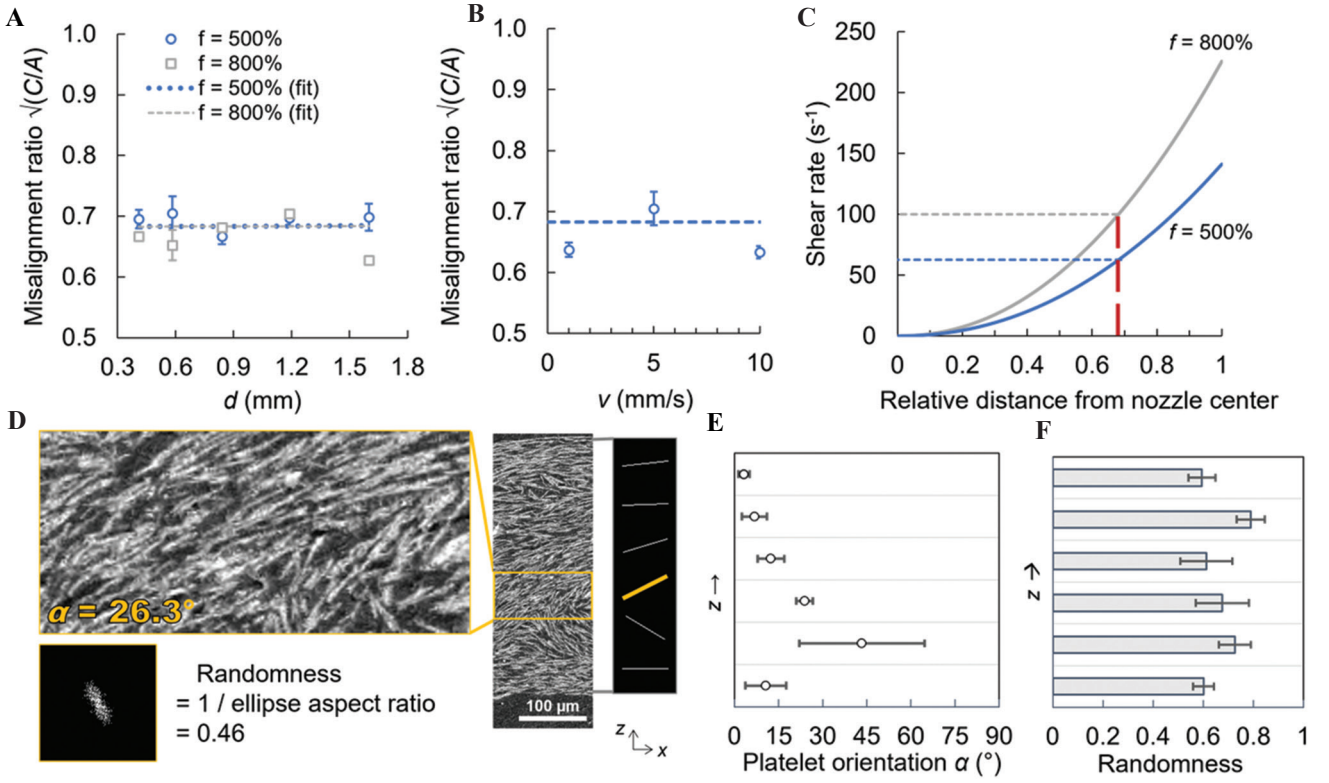

Figure 6. (A) Misalignment ratio $\sqrt{C/A}$ as a function of the nozzle diameter *d*. *v* = 5 mm/s. (B) Misalignment ratio $\sqrt{C/A}$ as a function of the printing speed *v*. *d* = 0.58 mm, *f* = 500%. (C) When the flow rate multiplier *f* is increased from 500% to 800%, the misalignment ratio remains unchanged as shown by the red dashed line. (D) Scanning electron micrograph of the filament cross-section in *x*-*z* plane after calcination (*d* = 0.58 mm, *f* = 500%, *v* = 5 mm/s). Applying FFT to each segment gives the dominant platelet orientation *α* and the randomness of alignment. The six lines on the right represent the typical platelet orientation in the six segments. (E) Dominant platelet orientation *α* in each of the six segments, taken as a positive value from the x-axis, along the height *z* of the filament. (F) Randomness of platelet alignment in each segment along the height (1 = completely random).

alumina ink[27]. This indicates that the platelet alignment process during printing is predictable and independent from the printing parameters. To study this, the ink can be simplified to rigid disc-shaped particles suspended in an incompressible Newtonian fluid undergoing laminar flow down a long pipe. Here, the nozzle is modeled as a long pipe relative to the particle size. The Newtonian fluid refers to the 7% PVP solution, while the brushite ink is non-Newtonian. As the ink flows down the nozzle, the particles nearest to the nozzle wall experience the maximum shear rate, following[33]:

$$\dot{\gamma}_{wall} = \frac{32Q}{\pi d^3} \tag{3.3}$$

while the particles at the nozzle center experience zero shear stress. The volumetric flow rate Q was determined experimentally by measuring the plunger speed. For a given printing speed v, Q increases linearly with the nozzle size d and the flow rate multiplier f (**Supplementary File: Section 3.1**). The time taken for the ink to travel down the nozzle was also calculated from the plunger speed. Then, the higher the shear rate experienced by a particle in the pipe, the shorter the time it takes to reach the equilibrium orientation, in this case tangential to the nozzle wall. This alignment time t_a is inversely proportional to the shear rate $\dot{\gamma}_a$ [37], following:

$$t_a \propto \frac{1}{\dot{\gamma}_a} \tag{3.4.}$$

Since this approximation in Equation 3.4 holds for particles at high solid loadings and low shear rate[37], the relationship in Equation (3.4) can be applied to brushite ink. Given that the shear stress τ decreases linearly from τ_{wall} at the nozzle wall to zero at the nozzle center, the shear stress at any position along the nozzle diameter can now be determined[28,37]. We then used the misalignment ratio $\sqrt{(C/A)}$, which estimates the relative core radius, to determine the shear stress τ at the core-shell border.

$$\tau_a = \sqrt{\frac{C}{A}} \times \tau_{wall} \tag{3.5}$$

Through the Herschel-Bulkley relation, the minimum shear rate required to align brushite microplatelets is hence determined.

$$\dot{\gamma}_a = \left(\frac{\tau_a - \tau_y}{K} \right)^{\frac{1}{n}} \quad (3.6.)$$

Platelets in the core experienced $\dot{\gamma} < \dot{\gamma}_a$ in the nozzle and hence remained disordered upon extrusion, while platelets in the shell experienced $\dot{\gamma} > \dot{\gamma}_a$ and preferentially aligned to the nozzle wall. Indeed, our observations of the misalignment ratio at different print parameters obey the model described by Equation 3.4 (**see Supplementary File: Section 1.2 and 3.2** for details on the model). Furthermore, our experimental results showed that $t_a \propto 1/d$ (see **Supplementary File: Section 3.2**) and we therefore obtain the following relation:

$$\dot{\gamma}_a \propto \frac{1}{t_a \times d} \quad (3.7)$$

Although changing the print parameters such as flow rate multiplier *f* or the nozzle diameter *d* changes the volume flow rate *Q* and shear stress, the misalignment ratio remains constant since t_a changes at the same time. For example, when *f* is increased from 500% to 800% (**Figure 6C**), the increase in *Q* leads to the higher shear stress and shear rate experienced by the platelets in the nozzle, so the required alignment time t_a is reduced. At the same time, the increased ink extrusion rate provides less time for platelets to rotate and align to the equilibrium orientation, resulting in an unchanged misalignment ratio when *f* increased. Therefore, the filament microstructure is unaffected by printing parameters and is expected to depend solely on the ink's rheology. For a given ink, this enables design flexibility at the macro-level (print resolution and print speed) without affecting the core-shell microstructure. Furthermore, with the help of the model and the possibility to relate the rheological properties to the microstructure, it should be possible to design inks to obtain specific microstructures. For example, to tune the misalignment ratio, the viscosity could be modified by fine tuning the concentration in PVP in the ink, without modifying the concentration of CaP microplatelets.

To confirm the platelet orientation inside a printed filament, SEM micrographs of the *x-z* cross-section of those filaments were examined (**Figure 6D**). Gradient changes in the platelet orientation from the bottom of the filament to the middle and from the middle to the top were observed, as expected from the gradient increase in shear stress towards the filament edges due to the laminar flow. To quantify the change in platelet orientation, the electron micrographs of each filament were divided into six segments of equal height from bottom to top, and the platelet orientation and the degree of alignment in each segment were quantified by Fast Fourier Transformation (FFT). The FFT results for filaments extruded at d = 0.58, f = 500%, v = 5 mm/s in the +*x* direction are presented in **Figures 6D-F**. Taking the representative platelet orientation α of each segment; we can visualize the gradient platelet orientation in a typical filament. At the bottom of the filament, CaP platelets were oriented close to 0°, almost parallel to the print substrate (**Figure 6E**). The angle α increased sharply to 45° before decreasing gradually to ~0° near the top. Indeed, the platelets preferentially aligned with the extrusion direction, especially near the nozzle wall where the shear stresses are highest. Platelets at the bottommost and topmost segments also displayed the most uniform alignment (**Figure 6F**). Filaments extruded at different print parameters are expected to exhibit similar trends since their misalignment ratio is about the same.

Having studied the microstructure within one single printed filament, we now look at complex 3D prints to show how our 3D printing approach can be used to construct multi-layered bulk or porous, overhanging structures, while retaining the core-shell microstructure.

3.4. Building microstructured multi-layered structures

(1) Buildability of microstructured CaP

Moving from single filaments, we explored the capability of the printing strategy to build microstructured multi-layered structures. Thanks to the drying method, good buildability of multi-layered structures from 21 vol% brushite ink was possible at room temperature. **Figure 7A** shows that multi-layered parts have the core-shell microstructure like in single filaments (**Figure 5A**). The post-calcination layer height is ~0.5 mm using the nozzle of 0.58 mm diameter at f = 500% (**Figure 7A**).

Since solvent removal by capillary action starts at the substrate surface, it can be expected that there is a maximum height above which the drying takes too long to build more layers with good filament shape fidelity. In practice, this issue can be circumvented through combination with evaporative drying using a fan, heating gun, infrared lamp, or in an environment with controlled temperature. **Figure 7B** shows a thin wall 6 layers tall printed at room temperature at v = 5 mm/s. By heating gypsum on a hot plate, a 20-layer tall thin wall can be built at v = 1 mm/s (**Figure 7C**). In **Figure 7D**, a small jigsaw piece ten layers thick was printed on heated gypsum, showing the construction of intricate parts for custom repairs. Indeed, print fidelity on heated gypsum enables near net shape fabrication of ceramics.

(2) Porosity and print resolution

β-CPP has similar osteoinductivity as hydroxyapatite, and a biodegradability rate between hydroxyapatite and β-tricalcium phosphate (β-TCP and Ca_3PO_4)[38]. The resorption rate is dependent on the crystallographic structure which could be altered by sterilization and other

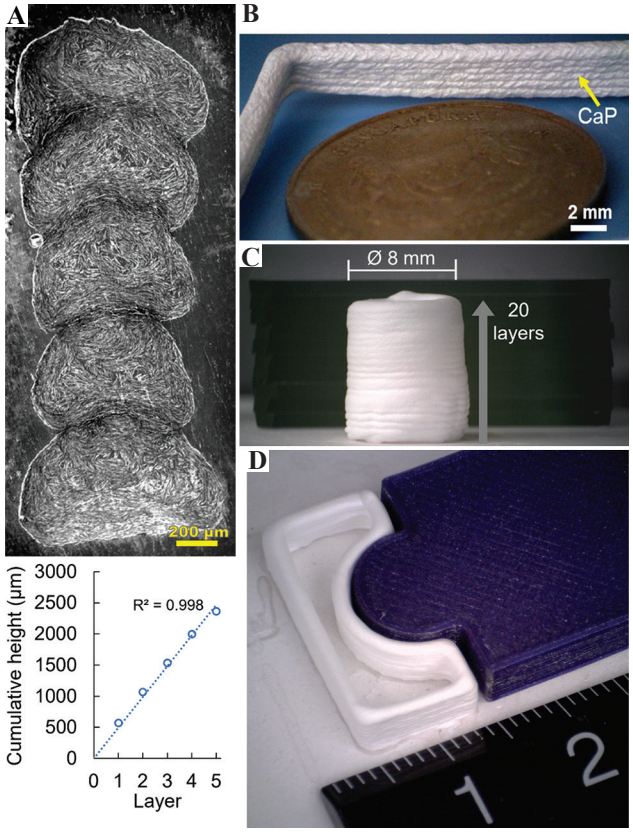

Figure 7. (A) Electron micrograph of the cross-section of a 5-layer print, scale bar: 200 µm. Height of calcined parts, printed at room temperature, d = 0.58 mm, f = 500%, v = 5 mm/s. Dashed line shows linear fit. (B) Optical photograph of a 6 layer-print after debinding, placed next to a Singapore 5-cent coin 16.75 mm in diameter. (C) Optical photograph of a 20-layer brushite cylindrical shell printed on heated gypsum. Background contains a stack of ten microscope glass slides 10.25 mm tall. (D) 10-layer brushite jigsaw piece printed on heated gypsum (left). 5 mm thick jigsaw piece printed from PLA by FDM (right). Ruler in centimeters.

processes[39]. Implantation in sheep tibiae found that the addition of 28 wt% CPP to brushite bone cement promoted bone mineralization *in vivo* as osteoblasts hydrolyzed pyrophosphate into orthophosphate ions[40]. Better osseointegration of bioceramics with pyrophosphate and bone mineralization in humans have also been clinically reported[39]. Prolonged exposure to pyrophosphate was found to stimulate osteoblast differentiation *in vitro*[39]. The bioactivity of β-CPP makes it a potential material in applications such as porous bone scaffolds, bone screws, bone coatings or bone plates. Osseointegration of CaP-based bone plates could potentially eliminate the need for surgical removal of metallic internal fixation.

To demonstrate various biomedical applications requiring different macro-porosity, multi-layered structures were designed with different infill density. In the first example, a 16 mm diameter scaffold resembling commonly robocast porous cancellous bone scaffolds was printed on heated gypsum (**Figure 8A**). At 30% infill density, filaments were widely spaced apart, which is expected to be favorable for vascularization (**Figure 8B**, **left**). In the second example, a higher infill density of 50% was used to print a six-layer thick portion of a bone plate at room temperature (**Figure 8B, right**). The outer surface finish appeared rough, as further discussed in **Supplementary File: Section: 4.2.** Post-processing would be required to improve the surface finish although surface roughness could promote cell attachment and bone growth[7]. Micro-porosity could be further explored using sacrificial organic material or foaming agents, for example. The effects of the scaffold microstructure and surface roughness on osteoinductivity, cell differentiation and proliferation, and bone remodeling remains to be explored.

Furthermore, our approach also permitted the printing of overhanging filaments that support their own weight. In our buildability test modified from Ribeiro *et al.* (2018)[41], underlying supports of three layers tall were extruded at spacing's ranging from 1.0 mm to 3.0 mm (**Figure 8C**). The fourth and topmost layer of filaments spanned across the supports below. Filaments extruded through 0.58 mm nozzle at f = 500% could be continuously extruded across supports up to 2.8 mm apart reliably. The topmost layer was able to support the weight of additional filaments without collapse and the filaments did not show deformation (see **Figure S6** in **Supplementary File**). Besides, the rectangular shape of majority of the pores as seen from the top view also points to good print accuracy and print fidelity[42]. 24 vol% brushite ink with higher storage modulus is expected to bridge wider spans[43].

For a 0.58 mm nozzle using flow rate of 500%, filament fusion occurred for center-to-center spacing of 1.0 mm (**Figure 8C**). The post-calcination filament width is 0.92 ± 0.03 mm. The horizontal print resolution is limited by the filament thickness after extrusion, which has a minimum of 0.7 mm in the green body for a nozzle diameter of 0.41 mm and flow rate of 400%. Although line-by-line robocasting is generally not well-suited for printing dense monolithic structures due to voids between printed filaments[30,36,44], we could make use of filament fusion to minimize porosity in bulk structures by careful tuning of the infill density I_f. At infill density I_f = 30%, there was no overlap between adjacent filaments. At $I_f \geq$ 70%, the overlap between adjacent filaments caused the layer height to increase unevenly, leading to deviation from the print design (**Figure 8D and E**). Infill density ~50% could be chosen to print bulk structures with minimal porosity and good interfilament interface (**Figure 8F**), It is also notable that the calcination step of the multi-layered bulk parts did not cause defects such as microcracks or delamination due to the consolidation without shrinkage. Anisotropic ceramic materials present a tendency to exhibit strong anisotropic shrinkage. This is

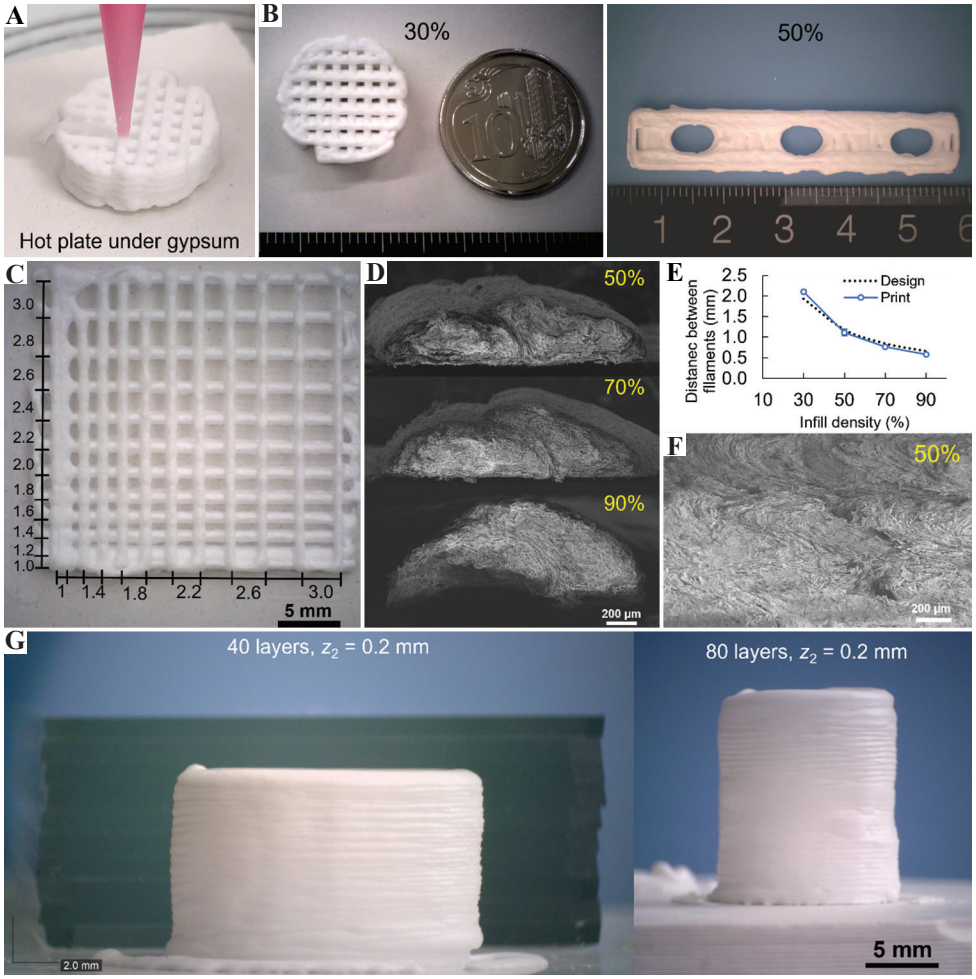

Figure 8. (A) Printing of 16 mm diameter scaffold on heated gypsum at v = 1 mm/s. (B) Brushite green body of 16 mm diameter scaffold next to a coin 18.5 mm in diameter (left). Brushite green body six layers thick resembling part of a bone plate (right). Ruler in centimeters. (C) Green body of 4-layer tall print on gypsum. Top layer of filaments spans across underlying supports at various distances apart (labeled in black in mm). d = 0.58 mm, f = 500%. (D) Cross-section of adjacent filaments printed at different infill density I_f. Scale bar: 200 µm. (E) Deviation of printed green body from design at different infill density. (F) Electron micrograph of dense bulk part printed at infill density of 50%. Scale bar: 200 µm. (G) Brushite cylindrical shells printed on heated gypsum at d = 1.19 mm, $z_1 = z_2$ = 0.2 mm, and v = 1 mm/s. Left: 40 layers tall. Background contains ten microscope slides 10.25 mm tall. Scale bar: 2 mm. Right: 80 layers tall. Scale bar: 5 mm.

mitigated here by the use of a mild heating and cooling ramp.

Replacing the 0.58 mm nozzle with a 1.19 mm nozzle, the layer height is reduced from ~0.5 mm (**Figure 7A and B**) to just ~0.2 mm (**Figure 8G**). In this way, the vertical resolution and side profile surface finish may be further improved by adjusting print parameters to reduce the layer height, with potential trade-offs in horizontal print resolution.

Our results demonstrate the ability to 3D print porous microstructured scaffolds from our CaP ink, which is a desired feature for biomedical applications. The dimensions are comparable to robocast CaP scaffolds, with a layer thickness 0.15~0.35 mm and a macro-pore width of 0.1~0.5 mm commonly reported[45]. Closed porosity does not contribute to a scaffold's nutrient exchange and generally weakens bulk ceramics exponentially. Notably, printing 21 vol% CaP ink at infill density ~50% eliminated internal voids, which are inevitable in conventional robocasting, while still being sufficiently printable. With our 3D printing method, it is, therefore, possible to design and print various complex 3D shapes, with well-controlled macroscopic porosity locally.

CaP materials like β-CPP are inherently brittle in the bulk, monolithic form, despite high stiffness of microplatelets at the nano-scale. Debinding and calcination at high temperatures removes all organic matter, so microstructured CaP scaffolds are fragile and brittle due to the absence of intermolecular forces or polymer chains bridging the CaP microplatelets. To induce toughening mechanisms, the residual open porosity obtained after calcination could be infiltrated

with a polymer having good interfacial strength with CaP. Based on the tension-shear chain model, the ceramic composite is expected to absorb energy as the polymer deforms until eventual platelet pull-out[3].

In addition, microstructure design is often used to toughen such ceramic composites. The periodic orientation of microplatelets in the printed multi-layered CaP (**Figure 8F**) bears resemblance to the periodic structures in highly tough natural materials often employed in biomimetic materials for toughness enhancement, such as the Bouligand structure[46]. We indeed found that the graded orientation of the microplatelets was effective and driving the crack along curved path, following the orientation of the planes of the microplatelets (see **Supplementary File: Section 5** for images of an unusual, curved crack path).

4. Conclusion

In this paper, we have developed an ink composition and 3D printing strategy to build complex shaped microstructured CaP-based materials. Aqueous inks containing CaP microplatelets were developed and their rheology studied. These inks were being dried upon deposition onto gypsum while simultaneously extruding the structure. We found that a concentration of 21 – 24 vol% CaP microplatelets was optimum for printing and studied the microstructure obtained in single filaments after calcination. In each filament, a core-shell microstructure with graded orientation of the microplatelets was obtained. Using a simple model to fit our results, we correlated the rheology of the ink to the microstructure so that it can be possible to further tune the ink composition to attain the desired core-shell microstructure. We also demonstrated porous scaffolds bridging 2.8 mm spans, as well as microstructured multi-layer structures. Such microstructured 3D printed green parts produce a bioresorbable material which make them interesting for biomedical applications such as hard tissue engineering. Micro-porosity could be further explored using sacrificial organic particles or polymer, or foaming agents, for example. Introduction of biological components and cell seeding post-calcination could be explored. Microstructure control is often used to toughen ceramic composites and previous work extruding water-based CaP ink without rheological modifiers did not produce microstructured filaments[47]. Polymer infiltration into the calcium pyrophosphate after calcination could enable toughening mechanisms in the resultant ceramic composite, such as crack bifurcation, platelet pull-out or polymer deformation. Thanks to this 3D printing method, it is now possible to build bulk microstructured CaP from low viscosity inks with a wide range of porosity. To enable CaP materials to be 3D printed into custom-shaped bioactive implants, scaffold macro-porosity will be tuned by computer-aided design (CAD) to study the influence of the CaP microstructure design on the mechanical properties of the infiltrated CaP composites.

Acknowledgments

The authors thank Chan Xin Ying for customizing the 3D printer. The authors would like to acknowledge the Facility for Analysis, Characterisation, Testing and Simulation, Nanyang Technological University, Singapore, for use of their electron microscopy and X-ray facilities.

Funding

This work was supported by the National Research Foundation, Singapore, with the Fellowship NRFF12-2020-0006.

Conflict of interest

The authors declare no conflict of interest.

Author contributions

D.P. and T.S. prepared the samples. T.S. performed experiments and SEM imaging. D.P. analyzed the data and drafted the manuscript. L.F.H. supervised the project, designed the experiments, and reviewed the manuscript

References

1. Reznikov N, Bilton M, Lari L, *et al.*, 2018, Fractal-like Hierarchical Organization of Bone Begins at the Nanoscale. *Science*, 360:eaao2189. https://doi.org/10.1126/science.aao2189
2. Beniash E, Stifler CA, Sun CY, *et al.*, 2019, The Hidden Structure of Human Enamel. *Nat Commun*, 10:1–13. https://doi.org/10.1038/s41467-019-12185-7
3. Gao H, 2006, Application of fracture mechanics concepts to hierarchical biomechanics of bone and bone-like materials. *Int J Fract*, 138:101–137. https://doi.org/10.1007/s10704-006-7156-4
4. Wegst UG, Bai H, Saiz E, *et al.*, 2015, Bioinspired Structural Materials. *Nat Mater*, 14:23–36. https://doi.org/10.1038/nmat4089
5. Yousefi AM, 2019, A Review of Calcium Phosphate Cements and Acrylic Bone Cements as Injectable Materials for Bone Repair and Implant Fixation. *J Appl Biomater Funct Mater*, 17:2280800019872594. https://doi.org/10.1177/2280800019872594
6. Jia W, Lau GY, Huang W, *et al.*, 2015, Bioactive Glass for Large Bone Repair. *Adv Healthc Mater*, 4:2842–2848. https://doi.org/10.1002/adhm.201500447

7. Marques A, Miranda G, Silva F, *et al.*, 2021, Review on Current Limits and Potentialities of Technologies for Biomedical Ceramic Scaffolds Production. *J Biomed Mater Res Part B Appl Biomater*, 109B:1–17. https://doi.org/10.1002/jbm.b.34706
8. Li T, Chang J, Zhu Y, *et al.*, 2020, 3D Printing of Bioinspired Biomaterials for Tissue Regeneration. *Adv Healthc Mater*, 9:1–17. https://doi.org/10.1002/adhm.202000208
9. Wen Y, Xun S, Haoye M, *et al.*, 2017, 3D Printed Porous Ceramic Scaffolds for Bone Tissue Engineering: A Review. *Biomater Sci*, 5:1690–8. https://doi.org/10.1039/C7BM00315C
10. Lin K, Sheikh R, Romanazzo S, *et al.*, 2019, 3D Printing of Bioceramic Scaffolds Barriers to the Clinical Translation: From Promise to Reality, and Future Perspectives. *Materials*, 12:2660. https://doi.org/10.3390/ma12172660
11. Le Ferrand H, Athanasiou CE, 2020, A Materials Perspective on the Design of Damage-Resilient Bone Implants Through Additive/Advanced Manufacturing. *JOM*, 72(3):1195–210. https://doi.org/10.1007/s11837-019-03999-3
12. Rogina A, Antunović M, Milovac D, 2019, Biomimetic Design of Bone Substitutes Based on Cuttlefish Bone-derived Hydroxyapatite and Biodegradable Polymers. *J Biomed Mater Res Part B Appl Biomater*, 107B:197–204. https://doi.org/10.1002/jbm.b.34111
13. Bigoni D, Cavuoto R, Misseroni D, *et al.*, 2020, Ceramics with the Signature of Wood: A Mechanical Insight. *Mater Today Bio*, 5:100032. https://doi.org/10.1016/j.mtbio.2019.100032
14. Sprio S, Panseri S, Montesi M*, et al.*, 2020, Hierarchical porosity inherited by natural sources affects the mechanical and biological behaviour of bone scaffolds. *Journal of the European Ceramic Society*, 40: 1717-1727. https://doi.org/10.1016/j.jeurceramsoc.2019.11.015
15. Tampieri A, Sprio S, Sandri M, *et al.*, 2011, Mimicking Natural Bio-mineralization Processes: A New Tool for Osteochondral Scaffold Development. *Trends Biotechnol*, 29:526–35. https://doi.org/10.1016/j.tibtech.2011.04.011
16. Ruffini A, Sprio S, Tampieri A, 2013, Study of the Hydrothermal Transformation of Wood-derived Calcium Carbonate into 3D Hierarchically Organized Hydroxyapatite. *Chem Eng J*, 217:150–8. https://doi.org/10.1016/j.cej.2012.11.107
17. Cheng Q, Huang C, Tomsia AP, 2017, Freeze Casting for Assembling Bioinspired Structural Materials. *Adv Mater*, 29:1703155. https://doi.org/10.1002/adma.201703155
18. Nelson I, Naleway SE, 2019, Intrinsic and Extrinsic Control of Freeze Casting. *J Mater Res Technol*, 8:2372–85. https://doi.org/10.1016/j.jmrt.2018.11.011
19. Deville S, Saiz E, Tomsia AP, 2006, Freeze Casting of Hydroxyapatite Scaffolds for Bone Tissue Engineering. *Biomaterials*, 27:5480–9. https://doi.org/10.1016/j.biomaterials.2006.06.028
20. Bouville F, Portuguez E, Chang Y, *et al.*, 2014, Templated Grain Growth in Macroporous Materials. *J Am Ceram Soc*, 97:1736–42. https://doi.org/10.1111/jace.12976
21. Bai H, Walsh F, Gludovatz B, *et al.*, 2016, Bioinspired Hydroxyapatite/Poly(methyl methacrylate) Composite with a Nacre-Mimetic Architecture by a Bidirectional Freezing Method. *Adv Mater*, 28:50–6. https://doi.org/10.1002/adma.201504313
22. Gao HL, Chen SM, Mao LB, *et al.*, 2017, Mass Production of Bulk Artificial Nacre with Excellent Mechanical Properties. *Nat Commun*, 8:287. https://doi.org/10.1038/s41467-017-00392-z
23. Chen SM, Gao HL, Zhu YB, *et al.*, 2018, Biomimetic Twisted Plywood Structural Materials. *Natl Sci Rev*, 5:703–14. https://doi.org/10.1093/nsr/nwy080
24. Kumar A, Kargozar S, Baino F, *et al.*, 2019, Additive Manufacturing Methods for Producing Hydroxyapatite and Hydroxyapatite-Based Composite Scaffolds: A Review. *Front Mater*, 6:1–20. https://doi.org/10.3389/fmats.2019.00313
25. Chen S, Jang TS, Pan HM, *et al.*, 2020, 3D Freeform Printing of Nanocomposite Hydrogels through in situ Precipitation in Reactive Viscous Fluid. *Int J Bioprint*, 6:29–49. https://doi.org/10.18063/ijb.v6i2.258
26. Martin JJ, Fiore BE, Erb RM, 2015, Designing Bioinspired Composite Reinforcement Architectures via 3D Magnetic Printing. *Nat Commun*, 6:1–7. https://doi.org/10.1038/ncomms9641
27. Feilden E, Ferraro C, Zhang Q, *et al.*, 2017, 3D Printing Bioinspired Ceramic Composites. *Sci Rep*, 7:1–9. https://doi.org/10.1038/s41598-017-14236-9
28. Fu Z, Freihart M, Wahl L, *et al.*, 2017, Micro-and Macroscopic Design of Alumina Ceramics by Robocasting. *J Eur Ceram Soc*, 37:3115–24. https://doi.org/10.1016/j.jeurceramsoc.2017.03.052
29. Le Ferrand H, 2020, Pressure-Less Processing of Ceramics with Deliberate Elongated Grain Orientation and Size. In:

Minerals, Metals and Materials Series. Berlin/Heidelberg: Springer. p45–56.
https://doi.org/10.1007/978-3-030-36552-3_5

30. Zocca A, Colombo P, Gomes CM, *et al.*, 2015, Additive Manufacturing of Ceramics: Issues, Potentialities, and Opportunities. *J Ame Ceram Soc*, 98:1983–2001.
https://doi.org/10.1111/jace.13700
31. Mandel S, Tas AC, 2010, Brushite ($CaHPO_4 \cdot 2H_2O$) to Octacalcium Phosphate ($Ca_8(HPO_4)_2(PO_4)_4 \cdot 5H_2O$) Transformation in DMEM Solutions at 36.5 °C. *Mater Sci Eng C*, 30:245–54.
https://doi.org/10.1016/j.msec.2009.10.009
32. Anastasiou AD, Thomson CL, Hussain SA, *et al.*, 2016, Sintering of calcium phosphates with a femtosecond pulsed laser for hard tissue engineering. *Mater Des*, 101:346–54.
https://doi.org/10.1016/j.matdes.2016.03.159
33. M'Barki A, Bocquet L, Stevenson A, 2017, Linking Rheology and Printability for Dense and Strong Ceramics by Direct Ink Writing. *Sci Rep*, 7:1–10.
https://doi.org/10.1038/s41598-017-06115-0
34. del-Mazo-Barbara L, Ginebra MP, 2021, Rheological Characterisation of Ceramic Inks for 3D Direct Ink Writing: A Review. *J Eur Ceram Soc*, 41:18–33.
https://doi.org/10.1016/j.jeurceramsoc.2021.08.031
35. Adcock D, McDowall I, 1957, The Mechanism of Filter Pressing and Slip Casting. *J Am Ceram Soc*, 40:355–60.
https://doi.org/10.1111/j.1151-2916.1957.tb12552.x
36. Hu F, Mikolajczyk T, Pimenov DY, *et al.*, 2021, Extrusion-based 3d Printing of Ceramic Pastes: Mathematical Modeling and *In Situ* Shaping Retention Approach. *Materials*, 14:1–22.
https://doi.org/10.3390/ma14051137
37. Hausmann MK, Rühs PA, Siqueira G, *et al.*, 2018, Dynamics of Cellulose Nanocrystal Alignment during 3D Printing. *ACS Nano*, 12:6926–37.
https://doi.org/10.1021/acsnano.8b02366
38. Windarti T, Taslimah, Haris A, *et al.*, 2017, Synthesis of β-Calcium Pyrophosphate by sol-gel method. *IOP Conf Ser Mater Sci Eng*, 172:012058.
https://doi.org/10.1088/1757-899X/172/1/012058
39. Pujari-Palmer M, Pujari-Palmer S, Lu X, *et al.*, 2016, Pyrophosphate Stimulates Differentiation, Matrix Gene Expression and Alkaline Phosphatase Activity in Osteoblasts. *PLoS One*, 11:e0163530.
https://doi.org/10.1371/journal.pone.0163530
40. Grover LM, Wright AJ, Gbureck U, *et al.*, 2013, The Effect of Amorphous Pyrophosphate on Calcium Phosphate Cement Resorption and Bone Generation. *Biomaterials*, 34:6631–7.
https://doi.org/10.1016/j.biomaterials.2013.05.001
41. Ribeiro A, Blokzijl MM, Levato R, *et al.*, 2018, Assessing Bioink Shape Fidelity to Aid Material Development in 3D Bioprinting. *Biofabrication*, 10:14102.
https://doi.org/10.1088/1758-5090/aa90e2
42. Schwab A, Levato R, D'Este M, *et al.*, 2020, Printability and Shape Fidelity of Bioinks in 3D Bioprinting. *Chem Rev*, 120:11028–55.
https://doi.org/10.1021/acs.chemrev.0c00084
43. Smay JE, Cesarano J, Lewis JA, 2002, Colloidal Inks for Directed Assembly of 3-D Periodic Structures. *Langmuir*, 18:5429–37.
https://doi.org/10.1021/la0257135
44. Li Z, Hojati M, Wu Z, *et al.*, 2020, Fresh and Hardened Properties of Extrusion-based 3D-printed Cementitious Materials: A Review. *Sustainability* (*Switzerland*), 12:1–33.
https://doi.org/10.3390/su12145628
45. Liu Q, Lu WF, Zhai W, 2021, Toward Stronger Robocast Calcium Phosphate Scaffolds for Bone Tissue Engineering: A Mini-review and Meta-analysis. *Mater Sci Eng C*, 107:2411–502.
https://doi.org/10.1016/j.msec.2021.112578
46. Behera RP, Le Ferrand H, 2021, Impact-resistant Materials Inspired by the Mantis Shrimp's Dactyl Club. *Matter*, 4:2831–49.
https://doi.org/10.1016/j.matt.2021.07.012
47. Houmard M, Fu Q, Saiz E, *et al.*, 2012, Sol-gel Method to Fabricate CaP Scaffolds by Robocasting for Tissue Engineering. *J Mater Sci Mater Med*, 23:921–30.
https://doi.org/10.1007/s10856-012-4561-2
48. Huang H, Lu X, 2017, An Ellipsoidal Particle in Tube Poiseuille Flow. *J Fluid Mech*, 822:664–88.
https://doi.org/10.1017/jfm.2017.298

Publisher's note